

Simultaneous Multi-Slice MRI using Cartesian and Radial FLASH and Regularized Nonlinear Inversion: SMS-NLINV

Sebastian Rosenzweig¹, H. Christian M. Holme^{1,2}, Robin N. Wilke^{1,2}, Dirk Voit³, Jens Frahm^{2,3} and Martin Uecker^{1,2}

¹Institute for Diagnostic and Interventional Radiology, University Medical Center Göttingen, Göttingen, Germany.

²German Centre for Cardiovascular Research (DZHK), Partner site Göttingen, Göttingen, Germany.

³Biomedizinische NMR Forschungs GmbH am Max-Planck-Institut für biophysikalische Chemie, Göttingen, Germany.

August 4, 2017

Running head: SMS Reconstruction Using Nonlinear Inversion

Address correspondence to:

Sebastian Rosenzweig
University Medical Center Göttingen
Institute for Diagnostic and Interventional Radiology
Robert-Koch-Str. 40
37075 Göttingen, Germany
sebastian.rosenzweig@med.uni-goettingen.de

Approximate word count: 153 (Abstract) 3470 (body)

Submitted to *Magnetic Resonance in Medicine* as a Full Paper.

Part of this work has been presented at the ISMRM Annual Conference 2016 (Singapore) and 2017 (Honolulu). This work was supported by a seed grant of the Physics-to-Medicine Initiative Göttingen (LM der Niedersächsischen Vorab).

Abstract

Purpose: The development of a calibrationless parallel imaging method for accelerated simultaneous multi-slice (SMS) MRI based on Regularized Nonlinear Inversion (NLINV), evaluated using Cartesian and radial FLASH.

Theory and Methods: NLINV is a parallel imaging method that jointly estimates image content and coil sensitivities using a Newton-type method with regularization. Here, NLINV is extended to SMS-NLINV for reconstruction and separation of all simultaneously acquired slices. The performance of the extended method is evaluated for different sampling schemes using phantom and in-vivo experiments based on Cartesian and radial SMS-FLASH sequences.

Results: The basic algorithm was validated in Cartesian experiments by comparison with ESPIRiT. For Cartesian and radial sampling, improved results are demonstrated compared to single-slice experiments, and it is further shown that sampling schemes using complementary samples outperform schemes with the same samples in each partition.

Conclusion: The extension of the NLINV algorithm for SMS data was implemented and successfully demonstrated in combination with a Cartesian and radial SMS-FLASH sequence.

Key words: simultaneous multi-slice, SMS, multi-band, regularized nonlinear inversion, NLINV, parallel imaging

Introduction

Accelerating image acquisition is of great importance in clinical magnetic resonance imaging (MRI). Parallel imaging exploits receive-coil arrays for acceleration. Conventional reconstruction methods for parallel imaging consist of a calibration from reference lines followed by linear reconstruction [1, 2, 3, 4]. In contrast, Regularized Nonlinear Inversion (NLINV) [5] does not require a calibration step but simultaneously computes image content and coil sensitivities from all available data. Because NLINV does not depend on the presence of explicit (Cartesian) calibration data, it is ideally suited for non-Cartesian parallel imaging. For example, NLINV is used in a highly accelerated real-time MRI method based on radial sampling [6].

Many applications require the acquisition of several slices. Simultaneous multi-slice (SMS) MRI [7] allows for significant scan time reductions and improved image quality [8, 9]. In SMS MRI several slices are excited at the same time and the resulting superposition is disentangled using special encoding schemes [10, 11] and/or the spatial encoding information inherent in receiver coil arrays [7]. The main benefit of accelerated SMS MRI over conventional single-slice imaging is the possibility to distribute undersampling among an additional dimension and exploit sensitivity encoding in all three dimensions which allows for higher acceleration factors [12, 13, 14, 15, 16, 17].

The aim of this work is to extend NLINV for the reconstruction of SMS data. First, the extension of the algorithm for Cartesian and radial sampling with arbitrary encoding in slice direction is introduced. For Cartesian data from an SMS-FLASH sequence, SMS-NLINV is compared to ESPIRiT [4]. For Cartesian and radial data, a single-slice measurement is compared to SMS acquisitions with equivalent or complementary samples in each partition. Accelerated SMS measurements of a human brain and a human heart are performed to show feasibility of in vivo scans.

Theory

Table 1 shows the notation used in this work.

SMS Encoding and Excitation Pulses

In SMS MRI, M partitions $p = 1, \dots, M$ are measured to get information about M parallel slices $q = 1, \dots, M$. Please note that a fully sampled acquisition with M partitions has M times the number of samples compared to a single-slice experiment, and the acceleration factor of an SMS experiment is then given by $R = N^{\text{full}}/N^{\text{red}}$, with $N^{\text{full/red}}$ the number of samples acquired in a full and undersampled partition measurement, respectively. Contrary to conventional multi-slice, in each partition measurement all M slices are excited simultaneously, i.e. superposed data are acquired. In the limit of small flip angles, an SMS radio frequency (RF) excitation pulse which excites M slices at positions

z_q and thickness Δz_q can be created by superposing conventional single-slice excitation pulses $B_{\text{rf}}^{(1)}(z_q, \Delta z_q)$. To generate differently encoded partitions a unitary $M \times M$ encoding matrix Ξ is included. The SMS RF excitation pulse for partition measurement p is then given by

$$\tilde{B}_{\text{rf},p}^{(M)}(z_1, \dots, z_M, \Delta z_1, \dots, \Delta z_M) := \sum_{q=1}^M \Xi_{pq} B_{\text{rf}}^{(1)}(z_q, \Delta z_q). \quad (1)$$

Let $\mathbf{y}_q := (y_q^1, \dots, y_q^N)$ be a vector which contains the k-spaces y_q^j of slice q and coils $j = 1, \dots, N$. Then, the encoded k-space of partition p is given by

$$\tilde{\mathbf{y}}_p := \sum_{q=1}^M \Xi_{pq} \mathbf{y}_q. \quad (2)$$

Although the derived SMS-NLINV algorithm is completely generic, we use the discrete Fourier-matrix for encoding in the scope of this work, i.e.

$$\Xi_{pq} = \exp\left(-2\pi i \frac{(p-1)(q-1)}{M}\right), \quad p, q = 1, \dots, M. \quad (3)$$

Image reconstruction

If the encoded k-spaces $\tilde{\mathbf{y}}_1, \dots, \tilde{\mathbf{y}}_M$ determined by the M partition measurements are fully sampled, the k-space of each slice can be recovered by applying the inverse of the encoding matrix

$$\mathbf{y}_q^{\text{avg}} := \sum_{p=1}^M \Xi_{qp}^{-1} \tilde{\mathbf{y}}_p. \quad (4)$$

Note that the k-spaces $\mathbf{y}_q^{\text{avg}}$ possess an SNR benefit of \sqrt{M} compared to single-slice experiments due to averaging given by Eq. (4) and because Ξ is unitary. Eq. (4) can also be applied to undersampled data if the same k-space positions are acquired for all partitions. The recovered (but still undersampled) k-spaces $\mathbf{y}_q^{\text{avg}}$ can then be processed using conventional single-slice reconstruction algorithms. This still leads to an SNR benefit, but the actual advantage of SMS - the acceleration in direction perpendicular to the slices - only comes into play when distinct samples are acquired for each partition. Then, Eq. (4) is no longer applicable and more elaborate SMS reconstruction approaches must be applied. A novel approach to tackle this reconstruction problem is introduced in the following.

Regularized Nonlinear Inversion (NLINV) [5] can be extended for the reconstruction of encoded SMS data [18]. In NLINV, the MRI signal equation is modeled as a nonlinear operator equation,

$$F(X) = \tilde{Y}. \quad (5)$$

X is the vector to be reconstructed. It contains the image content $m_q(\mathbf{r})$ and the N coil sensitivities $c_q^j(\mathbf{r})$, $j = 1, \dots, N$, for each of the M slices q , i.e. the stacked vector $X := (\mathbf{x}_1, \dots, \mathbf{x}_M)^T$ as a concatenation of the vectors $\mathbf{x}_q := (m_q, c_q^1, \dots, c_q^N)^T$. The vector \tilde{Y} contains the encoded k-spaces for all M partitions and all N channels, i.e. $\tilde{Y} := (\tilde{\mathbf{y}}_1, \dots, \tilde{\mathbf{y}}_M)^T$ with $\tilde{\mathbf{y}}_p := (\tilde{y}_p^1, \dots, \tilde{y}_p^N)^T$. Then, the nonlinear mapping function F is given by

$$F : X \mapsto \mathbf{P}\Xi \begin{pmatrix} \mathcal{F}(m_1 \mathbf{c}_1) \\ \vdots \\ \mathcal{F}(m_M \mathbf{c}_M) \end{pmatrix}, \quad \mathcal{F}(m_q \mathbf{c}_q) := \begin{pmatrix} \mathcal{F}(m_q c_q^1) \\ \vdots \\ \mathcal{F}(m_q c_q^N) \end{pmatrix}. \quad (6)$$

Here, \mathcal{F} is the (two-dimensional) Fourier transform and Ξ is an encoding matrix, e.g. Eq. (3). The projection matrix \mathbf{P} is defined by

$$\mathbf{P} := \begin{pmatrix} P_1 & & 0 \\ & \ddots & \\ 0 & & P_M \end{pmatrix}, \quad (7)$$

where P_p is the orthogonal projection onto the k-space trajectory used for partition $p = 1, \dots, M$. A more compact notation for Eq. (6) can be given by introducing the operator \mathcal{C} , which performs the multiplication of the object with the sensitivities:

$$F : X \mapsto \mathbf{P}\Xi \mathcal{F} \mathcal{C} X. \quad (8)$$

The forward operator F weights the magnetization m_q of slice q with the coil sensitivities $\mathbf{c}_q = (c_q^1, \dots, c_q^N)^T$ (\mathcal{C}), transforms into k-space (\mathcal{F}), encodes (Ξ) and samples (\mathbf{P}). The derivative DF and its adjoint DF^H will be used later to solve the inverse problem Eq. (5) and are given in the Appendix. Figure 1 shows a flow chart of the operators F , DF and DF^H .

Eq. (5) is highly underdetermined, hence prior knowledge has to be incorporated to prevent image content to be assigned to coil profiles and vice versa. While the image content can contain strong variations and edges, coil profiles in general are smooth functions, so a smoothness-demanding norm can be applied. Uecker et al. suggest a Sobolev norm

$$\|f\|_{H^l} := \|a(I - b\Delta)^{l/2} f\|_{L^2}, \quad (9)$$

with l a positive integer, I the identity matrix, a and b scaling parameters and $\Delta = \partial_x^2 + \partial_y^2$ the 2D Laplacian. Hence, in Fourier space the standard L2-norm has to be weighted by the additional term $a(1 + b\|k\|^2)^{l/2}$, which penalizes high spatial frequencies. This regularization is implemented by transforming $X = (\mathbf{x}_1, \dots, \mathbf{x}_M)^T$ using a weighting matrix \mathcal{W}^{-1} . We denote $X' := \mathcal{W}^{-1}X$ and $\mathbf{x}'_q := \mathcal{W}^{-1}\mathbf{x}_q = (m_q, c_q^1, \dots, c_q^N)^T$. This yields a transformed but equivalent system of equations

$$G(X') := F\mathcal{W}X' = \tilde{Y}, \quad (10)$$

which is solved using the Iteratively Regularized Gauss Newton Method (IRGNM).

As a first step, the IRGNM linearizes Eq. (10),

$$\tilde{Y} = DG|_{X'_n} dX' + GX'_n, \quad (11)$$

where X'_n is the estimate of the n^{th} Newton step and $DG|_{X'_n}$ is the Jacobian of G at X'_n . This equation is solved in the least-squares sense and with regularization using the Conjugate Gradient algorithm. The corresponding cost function to be minimized in every Newton step is

$$\Phi(dX') = \underset{dX'}{\operatorname{argmin}} \left(\|DG|_{X'_n} dX' - (\tilde{Y} - GX'_n)\|_{L^2}^2 + \beta_n \|X'_n + dX'\|_{L^2}^2 \right), \quad (12)$$

where the L2 penalty term $\beta_n \|X'_n + dX'\|_{L^2}^2 = \beta_n \|\mathcal{W}^{-1} X_{n+1}\|_{L^2}^2$, with $\beta_n = \beta_0 h^n$ and $h \in (0, 1)$, implies Tikhonov regularization.

Implementation for Cartesian and non-Cartesian Data

We assume Eq. (5) to be given in discretized form and all functions are represented by vectors of point values on a rectangular grid. For Cartesian sampling, \mathcal{F} can be implemented exactly as a discrete Fourier transform, and P_p is a diagonal matrix with ones at sample positions and zeros elsewhere. The 2D Fourier transform \mathcal{F} always appears in combination with the encoding matrix Ξ , which in this work is the discrete Fourier-matrix Eq. (3). Thus, $\Xi\mathcal{F}$ and its adjoint can simply be implemented as a three-dimensional Fast Fourier transform and its adjoint. Note, that the 2D Fourier transform \mathcal{F} is a discretized version of a continuous Fourier transform, whereas the Fourier-encoding Ξ is discrete by definition.

For non-Cartesian sampling, P_p projects onto arbitrary positions in k-space. As in non-Cartesian SENSE, $P\mathcal{F}$ can be implemented with a non-uniform Fourier transform [19]. The term $\mathcal{F}^H \Xi^H \mathbf{P} \Xi \mathcal{F}$ is the main operation which occurs in each iteration step. As described previously [20], it can be interpreted as a non-periodic convolution with a point-spread function (PSF) which has to be evaluated on a region with compact support defined by the field-of-view. Thus, an efficient implementation is achieved with the fast Fourier transform on a 2-fold enlarged grid to implement the non-periodic convolution using Toeplitz embedding. This requires only a minor modification of the Cartesian implementation which can then be used with data gridded once onto the Cartesian grid in a preparatory step and with a pre-computed PSF.

Sampling Schemes

All utilized Cartesian sampling patterns possess L_{ref} reference lines in the k-space center, whereas the periphery is undersampled by a factor R . For each of the M partition measurements we can use a distinct undersampling pattern. The CAIPIRINHA technique can improve the image quality for SMS acquisitions by acquiring alternating lines between each partition [14, 21]. Alternatively, in each partition the same samples can be acquired (aligned pattern).

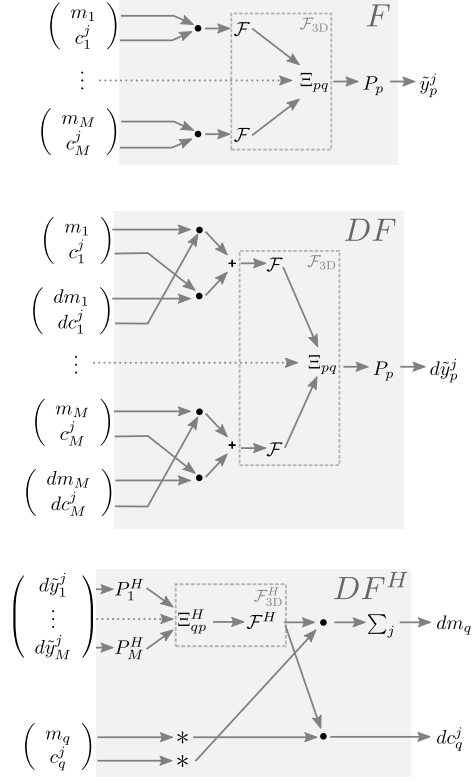


Figure 1: Flow chart for the calculation of the forward operator F , its derivative DF and the adjoint of the derivative DF^H . \tilde{y} : Encoded k-space data. m : Magnetization. c : Coil sensitivity. P : Projection onto k-space trajectory. \mathcal{F} : 2D Fourier transform. Ξ_{pq} : Encoding matrix. \cdot : Pointwise multiplication. $+$: Addition. $*$: Complex conjugation.

In radial measurements k-space samples are acquired along spokes. Let N_{sp} be the total number of acquired spokes per partition. Then, the angle between consecutive spokes of a partition is set to $\alpha_{\text{sp}} = 2\pi/N_{\text{sp}}$ which guarantees uniform k-space coverage and prevents strong gradient delay artifacts by opposing the acquisition direction of adjacent spokes. For each partition the k-space trajectory, i.e. the spoke distribution scheme, can be chosen individually. Figure 2 shows three possible spoke distribution schemes: (1) The aligned scheme acquires the same spokes for each partition. (2) In the linear-turn scheme the initial spoke pattern is rotated by

$$\alpha_{\text{trn}}^{\text{LIN}} = (p - 1) \cdot \frac{\pi}{N_{\text{sp}} \cdot M} \quad (13)$$

for partition $p = 1, \dots, M$, assuring the acquisition of complementary samples and uniform spoke distribution (cf. Fig. 2b). (3) Fourier-encoding in SMS MRI

can also be seen as an additional phase-encoding in k_z direction. The acquisition of many slices is therefore very similar to a stack-of-stars sequence in true 3D imaging for which Zhou et al. [22] showed that a golden angle-like rotation of the spoke distribution results in a higher image quality than aligned or linearly varied distributions. Here the turn angle for partition p is given by

$$\alpha_{\text{trn}}^{\text{GA}} = \left((p-1) \cdot \frac{\pi}{N_{\text{sp}}} \cdot \frac{\sqrt{5}-1}{2} \right) \bmod \frac{\pi}{N_{\text{sp}}}. \quad (14)$$

This scheme provides a more uniform local 3D k-space coverage as can be seen in Fig. 2c, but the spokes themselves are not as evenly distributed as in the linear-turn scheme. Turn-based spoke distribution schemes in combination with Fourier-encoded partition measurements are known to improve image quality similar to CAIPIRINHA in the Cartesian case [15, 21].

Post-processing

Although the matrix \mathcal{W} promotes adequate distribution of image content and coil sensitivities, the results may still exhibit minor large scale intensity variations compared to a conventional root-sum-of-squares (RSS) reconstruction. This can be compensated for by multiplying the image content with the RSS of the coil profiles:

$$m_q^{\text{final}} = m_q \cdot \sqrt{\sum_{j=1}^N |c_q^j|^2} \quad (15)$$

Methods

Cartesian and radial 2D FLASH sequences with adapted RF excitation pulses for Fourier-encoded SMS excitation as described in the theory section were developed and utilized in this study. All experiments were conducted on a Magnetom Skyra 3T (Siemens Healthcare GmbH, Erlangen, Germany) scanner using a 20-channel head/neck coil for phantom and human brain measurements and a combined thorax and spine coil with 26 channels for human heart measurements. All phantom measurements (FOV = $170 \times 170 \text{ mm}^2$, matrix size 192×192 , slice thickness $\Delta z = 6 \text{ mm}$) were performed on a custom-made phantom (Fig. 3) consisting of ABS bricks (LEGO) being immersed in pure water.

It is designed such that the proton density of the top and bottom part of the phantom differ distinctly from each other. This property can be used to demonstrate the capability of SMS-NLINV to disentangle simultaneously excited slices. The in-vivo brain measurements (FOV = $230 \times 230 \text{ mm}^2$, matrix size 192×192 , slice thickness $\Delta z = 4 \text{ mm}$, flip angle $\theta = 25^\circ$) as well as the heart measurements (FOV = $256 \times 256 \text{ mm}^2$, matrix size 160×160 , slice thickness $\Delta z = 6 \text{ mm}$, flip angle $\theta = 8^\circ$) were performed on volunteers with no known illnesses. In all experiments, all simultaneously acquired slices are separated by

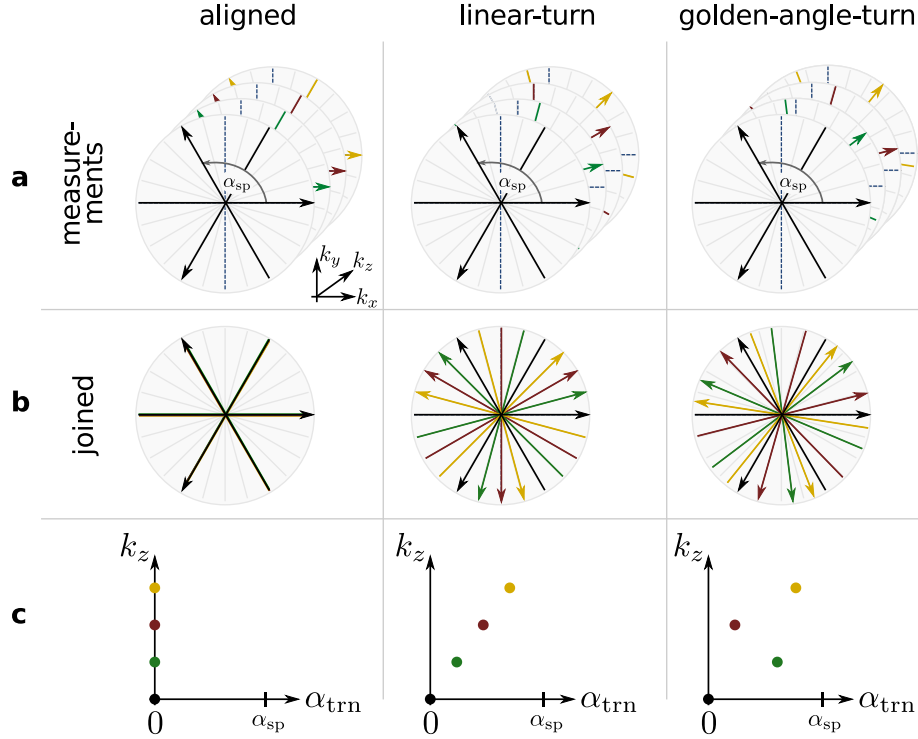


Figure 2: Schematic for three radial sampling schemes (multi-band factor $M = 4$ and $N_{\text{sp}} = 3$ spokes per partition measurement). Aligned: Same spokes acquired for each partition. Linear-turn: Linearly varied rotation angle α_{trn} of the initial spoke distribution. Golden-angle-turn: Rotation angle α_{trn} chosen according to the golden angle. a) Spoke distribution for all 4 partitions. α_{sp} is the angle between consecutive spokes. The arrow hints the readout direction. b) Spokes of all partitions plotted in one diagram. c) k_z plotted against the rotation angle α_{trn} .

a fixed distance d . NLINV as well as SMS-NLINV were implemented in the C-based software package BART [23]. The initial guess was $m_q = 1$ ($q = 1, \dots, M$) for the magnetizations and $c_q^j = 0$ ($q = 1, \dots, M, j = 1, \dots, N$) for the coil sensitivities. The parameters for the Sobolev norm were set to $a = 1$, $b = 220$ and $l = 32$. The initial regularization parameter was $\beta_0 = 1$ with reduction factor $h = 1/2$. In the interest of reproducible research, code and data to reproduce the experiments are made available on Github.¹

To confirm the basic functionality of SMS-NLINV, a Cartesian SMS measurement with multi-band factor $M = 2$ (slice distance $d = 60$ mm, TE/TR=4.4/8.3 ms, flip angle $\theta = 15^\circ$) was performed on the brick phantom. A full k-space was acquired and undersampling was performed retrospectively by multiplica-

¹<https://github.com/mrirecon/sms-nlinv>

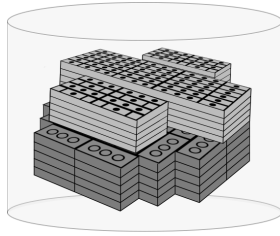


Figure 3: Schematic of the custom-made phantom consisting of LEGO bricks in pure water.

tion with the corresponding patterns. The full and a retrospectively undersampled k-space (CAIPIRINHA pattern, $R = 4$, $L_{\text{ref}} = 12$) were reconstructed with SMS-NLINV. For comparison, reconstructions were also performed using the L2-regularized ESPIRiT algorithm [4], which is based on SENSE [1] and can therefore also be applied to SMS data [14]. To validate the accuracy of the results, difference images between the full and undersampled reconstructions were calculated. To assure proper difference images for ESPIRiT reconstructions, the complex-valued slice-images were multiplied with the corresponding coil sensitivities followed by a RSS combination. The post-processing step in SMS-NLINV already compensates for intensity variations, thus adequate difference images can be calculated using the magnitude of the resulting images. We performed the same experiment using $L_{\text{ref}} = 4$ reference lines to demonstrate the advantage of SMS-NLINV over ESPIRiT given a very small calibration region.

The CAIPIRINHA technique can significantly improve the image quality of SMS experiments [14, 21]. We confirm these findings for SMS-NLINV by comparing retrospectively undersampled SMS measurements (TE/TR=4.8/9.1 ms, flip angle $\theta = 15^\circ$, $L_{\text{ref}} = 12$, $R = 4$) with CAIPIRINHA patterns to SMS measurements with aligned patterns using the multi-band factors $M = 2$ (slice distance $d = 60$ mm) and $M = 3$ (slice distance $d = 30$ mm). The absolute slice locations were chosen such that the outermost slices in both experiments were located at the same positions, which allowed a comparison of the respective slice images. A reference measurement was performed with each investigated slice acquired separately in a single-slice experiment and reconstructed with regular NLINV using equivalent reconstruction parameters. Apart from reduced SNR, the single-slice measurements should be identical to the acquisition with the aligned patterns.

The same experiment was performed using a radial trajectory to rule out errors with the radial SMS-FLASH sequence (TE/TR=2.0/3.1 ms, flip angle $\theta = 15^\circ$, $N_{\text{sp}} = 29$ spokes per partition) and the SMS-NLINV reconstruction for non-Cartesian data. Again, the improved k-space coverage of interleaved acquisitions, i.e. the use of linear-turn- and golden-angle-turn-based spoke distributions, should provide better results than aligned distributions or single-slice measurements with the same reduction factor. As a reference we performed single slice measurements on the same slices using $N_{\text{sp}} = 301$ spokes

to achieve Nyquist sampling even in the outer region of k-space. Finally, we present two in-vivo experiments. First, $M = 5$ slices (slice distance $d = 60$ mm, TE/TR=4.0/9.8 ms, $N_{\text{sp}} = 39$ spokes per partition) of a human brain were acquired using the golden-angle-turn scheme. Reconstructions were performed using SMS-NLINV and L2-ESPIRiT. Calibration using ESPIRiT requires a four step procedure: (1) the reconstruction of a fully-sampled Cartesian calibration regions using gridding (for all partitions) (2) disentangling of the partitions into slices using the inverse of matrix Ξ , (3) Fourier transformation back into a Cartesian k-space (for each slice), and (4) actual calibration from the Cartesian k-space data (for each slice). For this procedure to work, only the region in k-space which fulfills the Nyquist criterion in all partitions can be used. The size of the calibration region for ESPIRiT R_{cal} is limited by the Nyquist criterion and was calculated to be $R_{\text{cal}} = 35 \times 35$. Second, $M = 2$ slices (slice distance $d = 40$ mm, TE/TR=1.37/2.2 ms, $N_{\text{sp}} = 35$ spokes per partition) of a human heart were acquired without ECG-triggering [6]. To be able to reconstruct a single frame without temporal regularization or filtering, we combined 5 interleaves with 7 spokes per partition to obtain a single data set with 35 spokes per partition and linear-turn scheme.

Results

Cartesian data

Figure 4a shows ESPIRiT and SMS-NLINV reconstructions of a 4-fold undersampled Cartesian SMS measurement with multi-band factor $M = 2$ and $L_{\text{ref}} = 12$ reference lines. The SMS-NLINV algorithm can completely disentangle the superposed slices without significant artifacts after $it = 9$ Newton steps. The resulting image quality is equivalent to ESPIRiT. Figure 4a also depicts difference images of undersampled and full reconstructions for both methods. For better visibility the image intensity was increased by a factor of 5. In all difference images almost no residual image content can be observed and mostly noise is present, which means that almost all aliasing artifacts could be eliminated. The enhanced noise in the central region is a consequence of the specific Cartesian sampling pattern. Figure 4b shows the same reconstructions using a reduced calibration region. Whereas we find significant aliasing artifacts for ESPIRiT, SMS-NLINV still provides good results after $it = 10$ Newton steps.

Figure 5 shows SMS-NLINV reconstructions of Cartesian SMS acquisitions with multi-band factors $M = 2$ and $M = 3$ after $it = 10$ Newton steps using aligned and CAIPIRINHA patterns. As a comparison, the figure also depicts NLINV reconstructions of single-slice measurements for the same slices using $it = 10$ Newton steps. For both pattern types and multi-band factors the superposition can be completely disentangled and no severe undersampling artifacts are present. However, the image quality resulting from the CAIPIRINHA data is clearly superior to aligned SMS and single-slice data. Besides an SNR benefit, the images of aligned SMS do not show any advantages compared to the

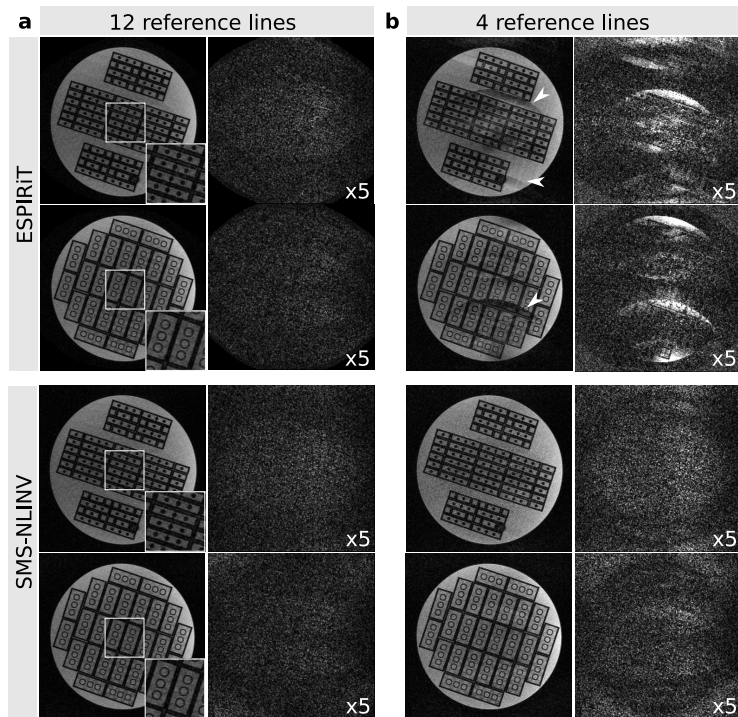


Figure 4: a) Reconstructions of a 4-fold undersampled Cartesian SMS measurement with multi-band factor $M = 2$ (slice distance $d = 60$ mm, $L_{\text{ref}} = 12$ reference lines) and corresponding difference images to full reconstructions: ESPIRiT and SMS-NLINV after $it = 9$ Newton steps. A magnified region-of-interest indicated by a white rectangle is shown as inset on the bottom right. For better visibility, the image intensity of the difference images was increased by a factor of 5. b) Same experiment as in a) using only $L_{\text{ref}} = 4$ reference lines and $it = 10$ Newton steps for SMS-NLINV. The arrows highlight aliasing artifacts.

single-slice images. By contrast, the CAIPIRINHA images resolve small details of the phantom bricks much better.

Radial data

Figure 6 depicts SMS-NLINV reconstructions of aligned, linear-turn- and golden-angle-turn-based radial SMS acquisitions with multi-band factor $M = 3$ after $it = 10$ Newton steps, as well as NLINV reconstructions of single-slice measurements for the same slices using $it = 10$ Newton steps. The results for $M = 2$ are provided as supporting Figure S1. Similar to Fig. 5 the slice images could be reconstructed without significant undersampling or superposition artifacts. As in the Cartesian case, the turn-based SMS acquisitions where complementary k-space data are acquired in each partition yield a much better image qual-

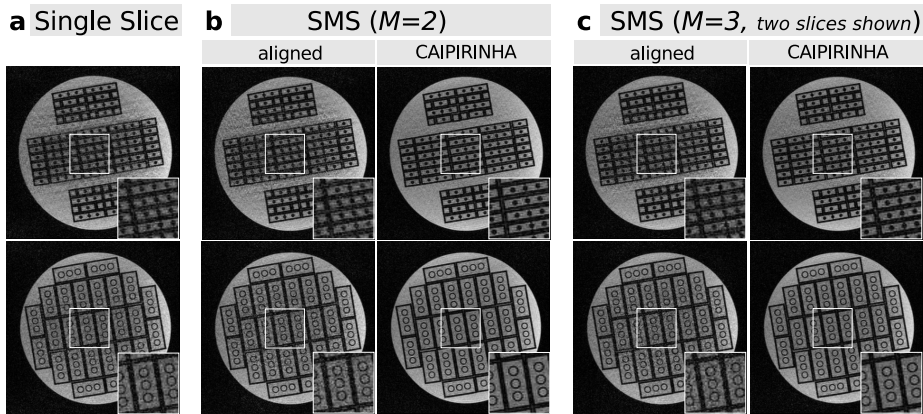


Figure 5: Comparison of different acquisition and reconstruction strategies for Cartesian measurements on the brick phantom with reduction factor $R = 4$ and $L_{\text{ref}} = 12$ reference lines. a) Single-slice acquisition and NLINV reconstruction for each slice. b) SMS acquisition and SMS-NLINV reconstruction for $M = 2$ and aligned (left) and CAIPIRINHA pattern (right). Slice distance $d = 60$ mm. c) SMS acquisition and SMS-NLINV reconstruction for $M = 3$ and aligned (left) and CAIPIRINHA pattern (right). Only the outermost slices with slice distance $d = 60$ mm are depicted. A magnified region-of-interest indicated by a white rectangle is shown as inset on the bottom right of every image.

ity than aligned SMS and single-slice measurements. The linear-turn and the golden-angle-turn scheme yield similar results. As supporting Figure S2 we provide difference images in image and k-space for $N_{\text{sp}} = 301$ and $N_{\text{sp}} = 29$ spokes per partition for the linear-turn-based $M = 3$ measurement. Supporting Figure S3 shows the same experiments as Figure 6 and supporting Fig. S1 but with $N_{\text{sp}} = 69$ spokes.

Figure 7 and 8 show the results of the in-vivo scans where we have chosen the number of Newton steps to obtain the best results using visual observation. Figure 7 shows $M = 5$ slices of a 7-fold undersampled acquisition of a human brain reconstructed with SMS-NLINV using $it = 11$ Newton steps and ESPIRiT. Both methods show similar results as all slices are completely disentangled and all streaking artifacts could be eliminated. As supporting Figure S4 shows, the residual for the SMS-NLINV reconstruction approaches a constant value when plotted against the number of Newton steps.

Figure 8 depicts $M = 2$ slices of a human heart in end-diastole simultaneously acquired in 154 ms using $N_{\text{sp}} = 35$ spokes per partition and reconstructed with SMS-NLINV using $it = 13$ Newton steps. Again, the two slices are completely disentangled and only slight blurring as well as minor streaking artifacts are present.

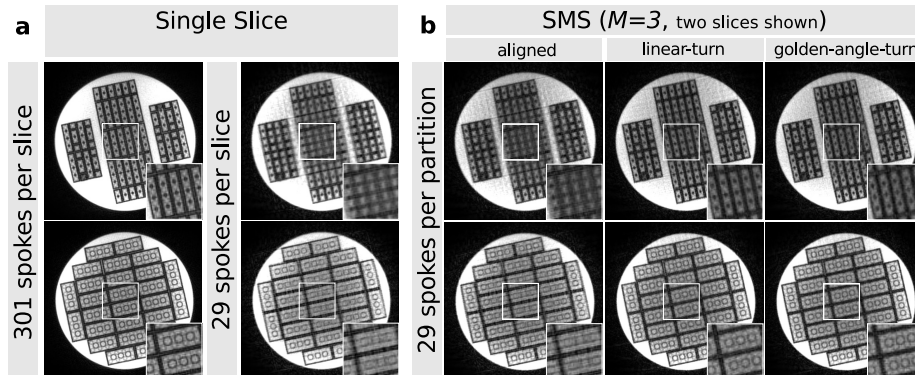


Figure 6: Comparison of different acquisition and reconstruction strategies for radial measurements on the brick phantom with $N_{\text{sp}} = 29$ spokes per partition or slice and a fully sampled reference scan with $N_{\text{sp}} = 301$ spokes per slice. a) Single-slice acquisition and NLINV reconstruction for each slice. b) SMS acquisition and SMS-NLINV reconstruction for $M = 3$ and aligned (left), linear-turn-based (center) and golden-angle-turn-based sampling (right). Only the outermost slices with slice distance $d = 60$ mm are depicted. A magnified region-of-interest indicated by a white rectangle is shown as inset on the bottom right of every image. The same experiment for $M = 2$ is provided as supporting Figure S1.

Discussion

In this work, SMS-NLINV has been combined with a Cartesian and a radial SMS-FLASH sequence.

With sufficient reference lines, SMS-NLINV and ESPIRiT reconstruct undersampled SMS data with similar image quality as shown in this work for radial and Cartesian data. This finding is in agreement with previous results comparing ESPIRiT and regular NLINV [4]. For very small calibration regions SMS-NLINV still provides good results where ESPIRiT reconstructions already show severe artifacts. The reason for this is that SMS-NLINV does not rely on a fully sampled calibration region but jointly estimates the image content and the coil sensitivities. In contrast, direct calibration using ESPIRiT or other calibration methods requires a complicated four step procedure and only the region in k-space which fulfills the Nyquist criterion simultaneously in all partitions can be utilized for calibration. SMS-NLINV not only makes all these additional separate processing steps unnecessary, it also works even for very small calibration regions by exploiting all available samples. This latter property makes SMS-NLINV ideally suited for non-Cartesian sampling, especially for accelerated dynamic imaging with changing coil sensitivities where only 5 to 7 spokes per partition are acquired and the Nyquist-sampled region can become very small [24]. We compared Cartesian SMS acquisitions with CAIPIRINHA and

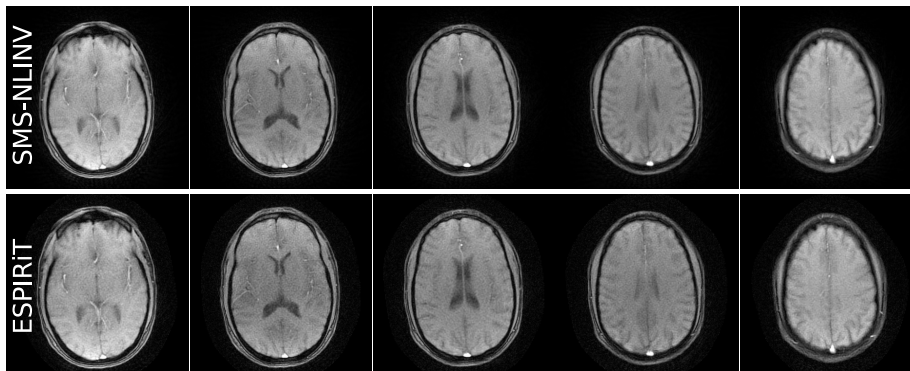


Figure 7: SMS-NLINV and ESPIRiT reconstructions of a human brain using a radial SMS-FLASH acquisition with multi-band factor $M = 5$ (slice distance $d = 10$ mm, slice thickness $\Delta z = 4$ mm, golden-angle-turn scheme, $N_{sp} = 39$ spokes per partition, $it = 11$ Newton steps).

aligned patterns as well as radial SMS acquisitions with aligned spoke scheme and linear-turn spoke schemes for different multi-band factors M with single-slice ($M = 1$) measurements as control. The aligned schemes acquire the same k-space samples for each of the M partitions which resembles an averaging process and thus yields an SNR benefit relative to single-slice measurements. However, the partitions do not contain complementary k-space information and therefore no significant advantages in terms of better resolved details can be achieved. In this case a joint reconstruction does not possess any benefits compared to an inverse discrete Fourier transform (Eq. (4)) on the Fourier-encoded k-spaces followed by single-slice reconstructions. The actual advantage of SMS-NLINV becomes apparent with the use of schemes where each partition contributes complementary k-space data which is equivalent to supplementary object information. Consequently, in addition to the SNR benefit, details are better resolved. Whereas single-slice NLINV and aligned SMS-NLINV recover missing k-space samples using 2D sensitivity information, SMS-NLINV using complementary data also exploits sensitivity variations in the third dimension which allows for higher acceleration factors [12].

In principle, the more slices M we simultaneously acquire using an interleaved scheme, the better will be the resulting image quality of each slice due to the \sqrt{M} -like SNR benefit and the acquisition of additional complementary samples. However, for the acquisition of M slices we have to perform M partition measurements and therefore the measurement time increases with increasing M until it approaches the time of a 3D measurement. The optimal choice for M depends on various experimental considerations such as overall motion robustness, magnetization preparation scheme, etc.

A future subject of study will be the use of SMS-NLINV for dynamic imaging at high temporal resolution, which was already successfully demonstrated for

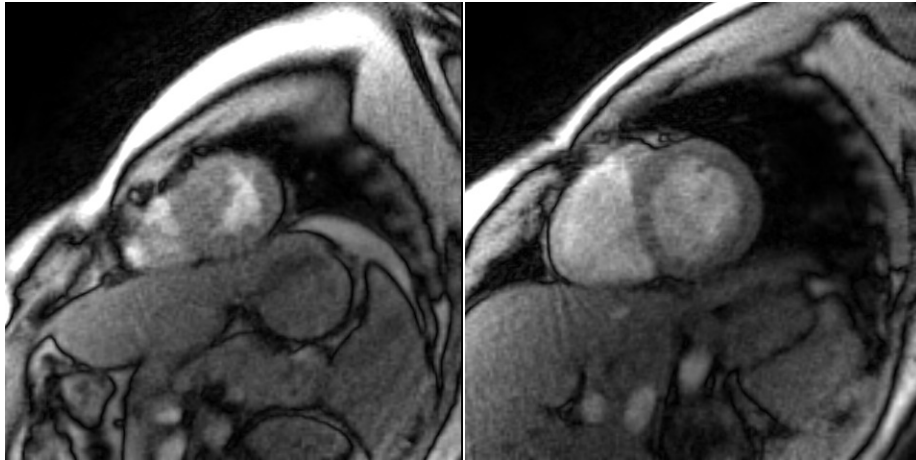


Figure 8: SMS-NLINV reconstruction of a human heart in end-diastole using a real-time SMS-FLASH acquisition with multi-band factor $M = 2$ (slice distance $d = 40$ mm, slice thickness $\Delta z = 6$ mm, $N_{\text{sp}} = 35$ spokes per partition, $it = 13$ Newton steps).

single-slice MRI using NLINV [25, 6, 26, 27]. The incorporation of additional minimization penalties such as temporal regularization and median filtering [25] known from NLINV and adapted spoke distribution schemes for dynamic SMS imaging [28] can directly be applied to SMS-NLINV and will further reduce streaking artifacts as well as blurring and improve the overall image quality. Preliminary results have been presented by Rosenzweig et al. [24].

In this work, we used a basic SMS-FLASH sequence. However, SMS-NLINV is a very general reconstruction approach and should be applicable to all sequences that can make use of an SMS acquisition, such as diffusion tensor imaging (DTI), functional MRI (fMRI) or T_1/T_2 quantification. In the future, we also plan to combine SMS-NLINV with a bSSFP sequence [29] and more advanced regularization techniques which will improve image quality at high acceleration [30, 31].

Conclusion

The present work extends the NLINV algorithm to simultaneous multi-slice MRI. As NLINV does not rely on the presence of Cartesian calibration data, it is an ideal choice for parallel imaging with non-Cartesian acquisitions. The combination with simultaneous multi-slice (SMS) offers the advantages of increased SNR and higher acceleration by exploiting three-dimensional sensitivity encoding.

Appendix

Glossary

Table 1: Glossary of notations

M	Multi-band factor
N	Number of receive channels
d	Slice distance
\mathbf{x}_q	Magnetization and coil sensitivities for slice q
\mathbf{y}	k-spaces of all coils
y^j	k-space of coil j
y_q	k-space of slice q
\mathbf{m}	Magnetizations seen by all coils
m^j	Magnetization seen by coil j
m_q	Magnetization of slice q
\mathbf{c}	Coil sensitivities of all coils
c_q	Coil sensitivity of slice q
\hat{c}	Normalized coil sensitivity
z_q	Center coordinate of slice q
Δz	Slice thickness
\sim	Encoded quantity
H	Adjoint
T	Transpose
$*$	Complex conjugate
it	Number of Newton steps.

Derivative and adjoint of the Forward operator

Given the forward operator $F(x)$ from Eq. (6) the corresponding derivative reads

$$DF|_X \begin{pmatrix} d\mathbf{x}_1 \\ \vdots \\ d\mathbf{x}_M \end{pmatrix} = \mathbf{P}\Xi \begin{pmatrix} \mathcal{F}(dm_1\mathbf{c}_1 + m_1d\mathbf{c}_1) \\ \vdots \\ \mathcal{F}(dm_M\mathbf{c}_M + m_Md\mathbf{c}_M) \end{pmatrix}. \quad (16)$$

The adjoint of the derivative is given by

$$DF^H|_X \begin{pmatrix} d\tilde{\mathbf{y}}_1 \\ \vdots \\ d\tilde{\mathbf{y}}_M \end{pmatrix} = \begin{pmatrix} \begin{pmatrix} \mathbf{c}_1^H \\ m_1^H \end{pmatrix} & & 0 \\ & \ddots & \\ 0 & & \begin{pmatrix} \mathbf{c}_M^H \\ m_M^H \end{pmatrix} \end{pmatrix} \mathcal{F}^H \Xi^H \mathbf{P}^H \begin{pmatrix} d\tilde{\mathbf{y}}_1 \\ \vdots \\ d\tilde{\mathbf{y}}_M \end{pmatrix}, \quad (17)$$

with

$$\begin{pmatrix} \mathbf{c}_q^H \\ m_q^H \end{pmatrix} := \begin{pmatrix} c_q^{1*}, \dots, c_q^{N*} \\ m_q^* \end{pmatrix}.$$

The asterisk * denotes pointwise complex conjugation.

Weighting Matrix

The weighting matrix used in SMS-NLINV to implement the smoothness penalty for the coil sensitivities is given by:

$$\mathcal{W}^{-1} := \begin{pmatrix} W^{-1} & & 0 \\ & \ddots & \\ 0 & & W^{-1} \end{pmatrix}, \quad (18)$$

Here, W^{-1} is the same weighting matrix as used in conventional NLINV:

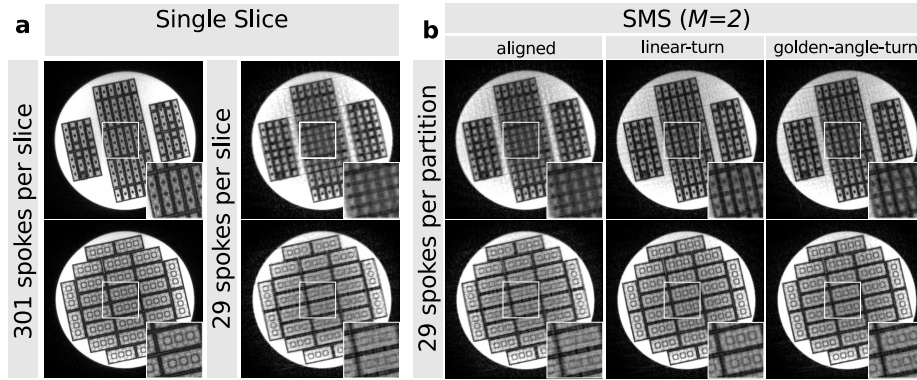
$$W^{-1} := \begin{pmatrix} I & & & 0 \\ a(1 + b\|\vec{k}\|^2)^{l/2} \mathcal{F} & & & \\ & \ddots & & \\ 0 & & & a(1 + b\|\vec{k}\|^2)^{l/2} \mathcal{F} \end{pmatrix}. \quad (19)$$

References

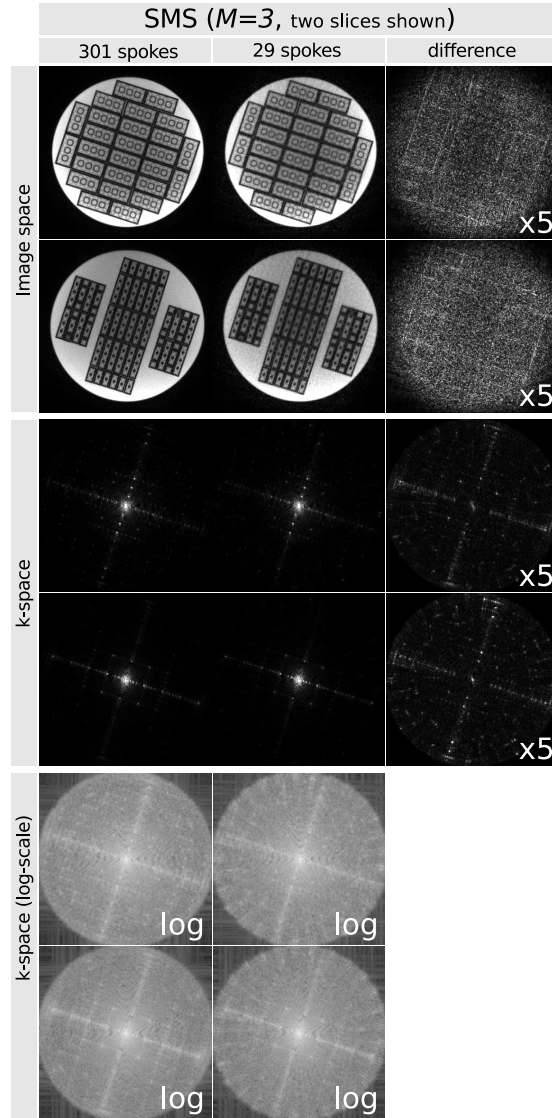
- [1] Pruessmann KP, Weiger M, Scheidegger MB, Boesiger P. SENSE: sensitivity encoding for fast MRI. *Magn. Reson. Med.* 1999; 42:952–962.
- [2] Griswold MA, Jakob PM, Heidemann RM, Nittka M, Jellus V, Wang J, Kiefer B, Haase A. Generalized autocalibrating partially parallel acquisitions (GRAPPA). *Magn. Reson. Med.* 2002; 47:1202–1210.
- [3] Lustig M, Pauly JM. SPIRiT: Iterative self-consistent parallel imaging reconstruction from arbitrary k-space. *Magn. Reson. Med.* 2010; 64:457–471.
- [4] Uecker M, Lai P, Murphy MJ, Virtue P, Elad M, Pauly JM, Vasanawala SS, Lustig M. ESPIRiT—an eigenvalue approach to autocalibrating parallel MRI: where SENSE meets GRAPPA. *Magn. Reson. Med.* 2014; 71:990–1001.
- [5] Uecker M, Hohage T, Block KT, Frahm J. Image reconstruction by regularized nonlinear inversion—joint estimation of coil sensitivities and image content. *Magn. Reson. Med.* 2008; 60:674–682.
- [6] Uecker M, Zhang S, Voit D, Karaus A, Merboldt KD, Frahm J. Real-time MRI at a resolution of 20 ms. *NMR Biomed.* 2010; 23:986–994.
- [7] Larkman DJ, Hajnal JV, Herlihy AH, Coutts GA, Young IR, Ehnholm G. Use of multicoil arrays for separation of signal from multiple slices simultaneously excited. *J. Magn. Reson. Imaging* 2001; 13:313–317.
- [8] Moeller S, Yacoub E, Olman CA, Auerbach E, Strupp J, Harel N, Ugurbil K. Multiband multislice GE-EPI at 7 tesla, with 16-fold acceleration using partial parallel imaging with application to high spatial and temporal whole-brain fMRI. *Magn. Reson. Med.* 2010; 63:1144–1153.
- [9] Feinberg DA, Moeller S, Smith SM, Auerbach E, Ramanna S, Glasser MF, Miller KL, Ugurbil K, Yacoub E. Multiplexed echo planar imaging for sub-second whole brain fMRI and fast diffusion imaging. *PLoS One* 2010; 5:e15710.
- [10] Maudsley AA. Multiple-line-scanning spin density imaging. *J. Magn. Reson.* 1980; 41:112–126.
- [11] Souza SP, Szumowski J, Dumoulin CL, Plewes DP, Glover G. SIMA: simultaneous multislice acquisition of MR images by Hadamard-encoded excitation. *J. Comput. Assist. Tomogr.* 1988; 12:1026–1030.
- [12] Weiger M, Pruessmann KP, Boesiger P. 2D sense for faster 3D MRI. *Magn. Reson. Mater. Phys., Biol. Med.* 2002; 14:10–19.
- [13] Wiesinger F, Boesiger P, Pruessmann KP. Electrodynamics and ultimate SNR in parallel MR imaging. *Magn. Reson. Med.* 2004; 52:376–390.

- [14] Breuer FA, Blaimer M, Heidemann RM, Mueller MF, Griswold MA, Jakob PM. Controlled aliasing in parallel imaging results in higher acceleration (CAIPIRINHA) for multi-slice imaging. *Magn. Reson. Med.* 2005; 53:684–691.
- [15] Yutzy SR, Seiberlich N, Duerk JL, Griswold MA. Improvements in multi-slice parallel imaging using radial CAIPIRINHA. *Magn. Reson. Med.* 2011; 65:1630–1637.
- [16] Wang H, Adluru G, Chen L, Kholmovski EG, Bangerter NK, DiBella EVR. Radial simultaneous multi-slice CAIPI for ungated myocardial perfusion. *Magn. Reson. Imaging* 2016; 34:1329 – 1336.
- [17] Setsompop K, Gagoski BA, Polimeni JR, Witzel T, Wedeen VJ, Wald LL. Blipped-controlled aliasing in parallel imaging for simultaneous multislice echo planar imaging with reduced g-factor penalty. *Magn. Reson. Med.* 2012; 67:1210–1224.
- [18] Rosenzweig S, Uecker M. Reconstruction of multiband MRI data using Regularized Nonlinear Inversion. In: *Proc. Intl. Soc. Mag. Reson. Med.* 24, Singapore, 2016. p. 3259.
- [19] Knoll F, Clason C, Uecker M, Stollberger R. Improved Reconstruction in Non-Cartesian Parallel Imaging by Regularized Nonlinear Inversion. In: *Proc. Intl. Soc. Mag. Reson. Med.* 17, Honolulu, 2009. p. 2721.
- [20] Wajer FTAW, Pruessmann KP. Major speedup of reconstruction for sensitivity encoding with arbitrary trajectories. In: *Proc. Intl. Soc. Mag. Reson. Med.* 9, Glasgow, 2001. p. 0767.
- [21] Zhu K, Kerr A, Pauly JM. Autocalibrating CAIPIRINHA: Reformulating CAIPIRINHA as a 3D Problem. In: *Proc. Intl. Soc. Mag. Reson. Med.* 20, Melbourne, 2012. p. 0518.
- [22] Zhou Z, Han F, Yan L, Wang DJ, Hu P. Golden-ratio rotated stack-of-stars acquisition for improved volumetric MRI. *Magn. Reson. Med.* 2017; DOI: 10.1002/mrm.26625.
- [23] Uecker M, Ong F, Tamir JI, Bahri D, Virtue P, Cheng JY, Zhang T, Lustig M. Berkeley advanced reconstruction toolbox. In: *Proc. Intl. Soc. Mag. Reson. Med.* 23, Toronto, 2015. p. 2486.
- [24] Rosenzweig S, Holme HCM, Wilke RN, Uecker M. Simultaneous Multi-Slice Real-Time Imaging with Radial Multi-Band FLASH and Nonlinear Inverse Reconstruction. In: *Proc. Intl. Soc. Mag. Reson. Med.* 25, Honolulu, 2017. p. 0518.
- [25] Uecker M, Zhang S, Frahm J. Nonlinear inverse reconstruction for real-time MRI of the human heart using undersampled radial FLASH. *Magn. Reson. Med.* 2010; 63:1456–1462.

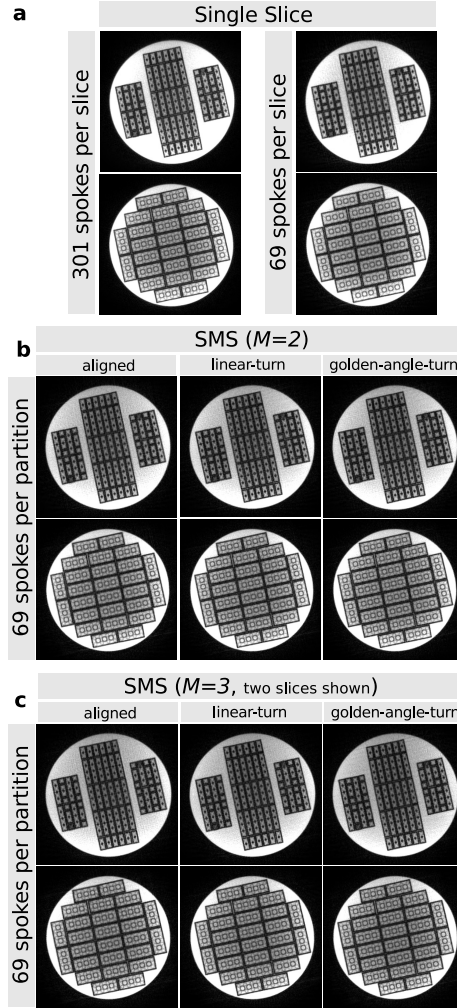
- [26] Voit D, Zhang S, UnterbergBuchwald C, Sohns JM, Lotz J, Frahm J. Real-time cardiovascular magnetic resonance at 1.5 T using balanced SSFP and 40 ms resolution. *J. Cardio. Magn. Reson.* 2013; 15:1–8.
- [27] Zhang S, Uecker M, Voit D, Merboldt K, Frahm J. Real-time cardiovascular magnetic resonance at high temporal resolution: radial FLASH with nonlinear inverse reconstruction. *J. Cardio. Magn. Reson.* 2010; 12:39.
- [28] Wu Z, Chen W, Khoo MCK, Davidson Ward SL, Nayak KS. Evaluation of upper airway collapsibility using real-time MRI. *J. Magn. Reson. Imaging* 2016; 44:158–167.
- [29] Stäb D, Ritter CO, Breuer FA, Weng AM, Hahn D, Köstler H. CAIPIR-INHA accelerated SSFP imaging. *Magn. Reson. Med.* 2011; 65:157–164.
- [30] Uecker M, Block KT, Frahm J. Nonlinear Inversion with L1-Wavelet Regularization – Application to Autocalibrated Parallel Imaging. In: *Proc. Intl. Soc. Mag. Reson. Med.* 16, Toronto, 2008. p. 1479.
- [31] Knoll F, Bredies K, Pock T, Stollberger R. Second order total generalized variation (TGV) for MRI. *Magn. Reson. Med.* 2011; 65:480–491.



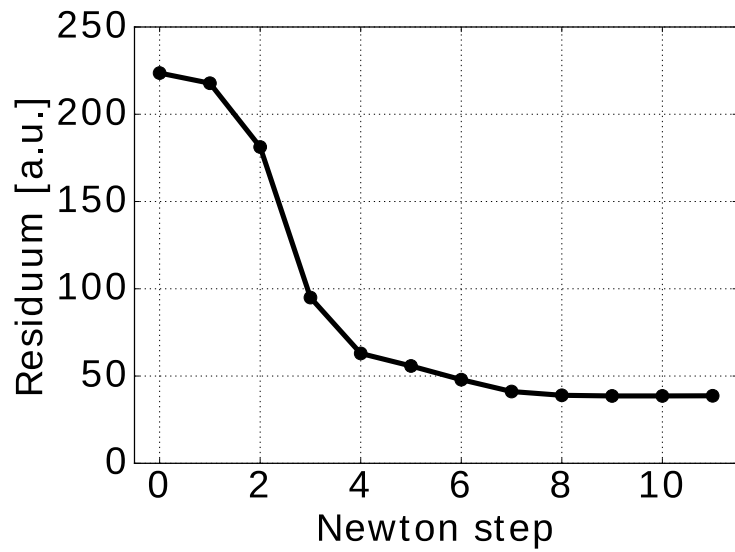
Supporting Figure S1: Comparison of different acquisition and reconstruction strategies for radial measurements on the brick phantom with $N_{\text{sp}} = 29$ spokes per partition or slice and a fully sampled reference scan with $N_{\text{sp}} = 301$ spokes per slice. a) Single-slice acquisition and NLINV reconstruction for each slice. b) SMS acquisition and SMS-NLINV reconstruction for $M = 2$ and aligned (left), linear-turn-based (center) and golden-angle-turn-based sampling (right). Slice distance $d = 60$ mm. A magnified region-of-interest indicated by a white rectangle is shown as inset on the bottom right of every image.



Supporting Figure S2: Difference images in image and k-space for SMS ($M = 3$, slice distance $d = 30$ mm, linear-turn-based spoke distribution) acquisitions with $N_{\text{sp}} = 301$ (fully sampled reference) and $N_{\text{sp}} = 29$ spokes per partition. For better visibility, the intensity of the difference images was increased by a factor of 5 and the k-spaces were additionally depicted using the log-scale.



Supporting Figure S3: Comparison of different acquisition and reconstruction strategies for radial measurements on the brick phantom with $N_{\text{sp}} = 69$ spokes per partition or slice and a fully sampled reference scan with $N_{\text{sp}} = 301$ spokes per slice. a) Single-slice acquisition and NLINV reconstruction for each slice. b) SMS acquisition and SMS-NLINV reconstruction for $M = 2$ and aligned (left), linear-turn-based (center) and golden-angle-turn-based sampling (right). Slice distance $d = 60$ mm. c) SMS acquisition and SMS-NLINV reconstruction for $M = 3$ and aligned (left), linear-turn-based (center) and golden-angle-turn-based sampling (right). Only the outermost slices with slice distance $d = 60$ mm are depicted.



Supporting Figure S4: Supporting Figure S4: Residuum of the SMS-NLINV reconstruction in Figure 7 against the number of Newton steps.